University of Birmingham

Distinct predatory behaviors in scimitar- and dirk-toothed sabertooth cats

Figueirido, Borja; Lautenschlager, Stephan; Pérez-Ramos, Alejandro; Van Valkenburgh, Blaire

[Link to publication on Research at Birmingham portal](#)

1 **Three-dimensional biomechanics reveals distinct predatory behaviors in scimitar- and**

2 **dirk-toothed sabertooth cats**

3

4 Borja Figueirido[1*], Stephan Lautenschlager[2], Alejandro Pérez-Ramos[1] and Blaire Van

5 Valkenburgh[3]

6

7 [1]Universidad de Málaga, Departamento de Ecología y Geología, Facultad de Ciencias, 29071-

8 Málaga, Spain.

9 [2]School of Geography, Earth and Environmental Sciences, University of Birmingham,

10 Edgbaston, Birmingham, B15 2TT, UK.

11 [3]Department of Ecology and Evolutionary Biology, UCLA, 621 Charles E Young Drive South,

12 Los Angeles, CA 90095-1606.

13

14 *author for corresponding: Borja.figueirido@uma.es

15

18

19 **SUMMARY**

20 Over the Cenozoic, large cat-like forms have convergently evolved into specialized killers of

21 'megaherbivores' that relied on their large, and laterally-compressed (saber-like) canines to

22 rapidly subdue their prey [1-5]. Scimitar- and dirk-toothed sabertooths are distinct ecomorphs

23 that differ in canine tooth length, degree of serration, and postcranial features indicative of

24   dissimilar predatory behavior [6-13]. Despite these differences, it is assumed that they used a

25   similar 'canine-shear' bite to drive their sabers through their prey [14,15]. We investigated the

26   killing behavior of the scimitar-toothed *Homotherium serum* and the dirk-toothed *Smilodon*

27   *fatalis* using a comparative sample of living carnivores and a new quantitative approach to the

28   analysis of skull function. For the first time, we quantified differences in the relative amount and

29   distribution of cortical (CB) and trabecular bone (TB) in coronal sections of skulls to assess

30   relative skull stiffness and flexibility [16-19]. We also use finite element analysis to simulate

31   various killing scenarios that load skulls in ways that are likely to favor distinct proportions of

32   CB/TB across the skull. Our data reveal that *S. fatalis* had an extremely thick skull and relatively

33   little TB, consistent with a large investment in cranial strength for a stabbing canine-shear-bite.

34   However, *H. serum* had more TB, and likely deployed an unusual predatory behavior that was

35   more similar to the clamp-and-hold technique of the lion than *S. fatalis*. These data broaden the

36   killing repertoire of sabertooths and highlight the degree of ecological specialization among

37   members of the large carnivore guild during the Late Pleistocene of North America.

38

39   **RESULTS**

40   *Profiles of CB and TB*

41   As CB tends to have high stiffness and TB has greater flexibility [16-19], we hypothesize that if

42   dirk-tooths and scimitar-tooths had distinctive killing bites that loaded their skulls differently,

43   they should diverge in the quantity and distribution of CB/TB as well. To test this, we quantified

44   the relative amount of cortical (CB) and trabecular bone (TB) of complete skulls of the two

45   sabertooths and three extant large carnivores, African lion (*Panthera leo*), spotted hyena

46   (*Crocuta crocuta*), and African wild dog (*Lycaon pictus*) (Fig. 1A; see methods for justification

47 of comparative sample). Our results reveal that the skulls of all species show two clear peaks in

48 CB surface area relative to the total area of the skull (RCBT) to varying degrees with the

49 exception of the wild dog (Fig. 1B, left). The first lies at the upper fourth premolar (carnassial),

50 and the second at the temporomandibular joint (TMJ). In the wild dog, the peak at the carnassial

51 is not pronounced, and CB area increases more gradually across the skull than in the feliforms

52 (Fig. 1B, left). Across all five species, there is considerable variation in the distribution of CB

53 surface area across the skull, with *S. fatalis* exceeding all species in the snout (slices #1-5;

54 Fig.1B; Fig. 2) except at the anterior-most point of the upper carnassial, where it is surpassed by

55 the spotted hyena (slice #3; Fig. 1B). The snout of *H. serum* has values of relative CB area that

56 are below those of *S. fatalis* except at slices #1 and #5, the anterior-most point of the canine and

57 the posterior-most point of the upper carnassial, respectively. Between those two positions, the

58 snout of *H. serum* is more similar to that of the extant lion in relative compact bone surface area

59 and much less than observed in the hyena and *S. fatalis*. (Fig. 1B, left). Beyond slice #5, both

60 saber-tooths have similar values of CB that fall below those of the wild dog and hyena

61 posteriorly (slices #5-10; Fig. 1B).

62   On a per slice basis, the proportion of CB (RCBS) fluctuates across the skull in all five

63 species, with all showing a decline at the TMJ (slice#8, Fig. 1C, left). Within the snout, the

64 proportion of CB per slice is greatest in the spotted hyena and *S. fatalis*, and least in the lion and

65 *H. serum* (Fig. 1C, left). Interestingly, the snout of the wild dog is similar to that of the spotted

66 hyena and *S. fatalis* in the proportion of compact bone at two anterior locations (slices #2-3), but

67 then declines for the remainder of the snout (slices #4-5; Fig. 1C, left).

68   TB surface area relative to total skull area (RTBT) in *S. fatalis* is most similar to that of

69 the spotted hyena, and to a lesser extent, *H. serum* and the wild dog (Fig. 1B, right). The lion

3

70   stands out with an unusually large proportion of TB at the TMJ (slice #8, Fig. 1B; Fig. 2) as well

71   as higher values at both the posterior margin of the upper carnassial/frontal region and behind the

72   TMJ (slices #4-5, 9-10; Fig 1B). The relatively large proportion of TB in the lion is confirmed in

73   the analysis of TB area per slice (RTBS), in which the lion displays an exceptionally large

74   proportion of TB per slice at the TMJ and caudal most position. (slice #8, 10, Fig. 1C). On a per

75   slice basis, the values for *H. serum* are also elevated and similar to those of the lion within the

76   anterior-most part of the snout (slices # 1-3; Fig. 1C). However, posteriorly (slices # 4-10; Fig.

77   1B), *H. serum* has relative TB area per slice values within the range of *S. fatalis* and all extant

78   species except the lion (slices # 5-10; Fig. 1B).

79

80   *Finite element analysis*

81   We used 3D biomechanical modelling to simulate a variety of killing scenarios, such as

82   stabbing or pulling back, that load skulls differently and therefore are likely to favor distinct

83   proportions of CB/TB across the skull. Biomechanical function and efficiency were assessed via

84   von Mises stress and displacement magnitudes in the different models/scenarios. Von Mises

85   stress is a scalar function of principal stresses (along orthogonal planes) and is a good predictor

86   of ductile material failure (20), whereas displacement magnitude indicates the deformation of

87   individual elements/regions due to external loading.

88   A comparison of von Mises stress values for each species under the four different loading

89   scenarios reveals that the skulls of the three felids undergo less stress during stabbing bites than

90   the skulls of either *Crocuta* or *Lycaon* (blue line, Fig. 3A). Of the three felids, *S. fatalis* exhibits

91   the least stress during a stabbing bite, followed closely by *H. serum* and then the lion.   However,

4

92   average values of node displacements under a stabbing load are very similar for both sabertooths

93   (Fig. 3B).

94   Contour plots of von Mises stress distributions reveal notable differences between *S.*

95   *fatalis* and *H. serum* during bilateral canine stabbing and pulling back. During bilateral canine

96   stabbing, both sabertooths are similar in showing relatively high stress across their braincase but

97   differ anteriorly, with *S. fatalis* exhibiting less stress across the rostrum than *H. serum* (Fig. 4).

98   However, the situation is different during the pull-back scenario, in which both show similar

99   stress in the rostrum but *S. fatalis* has greater stress across the braincase and zygomatics than *H.*

100   *serum*. All three of the extant species experience higher stresses during bilateral canine stabbing

101   than either of the saber-tooths (Fig. 4).

102   Mean von Mises stress values in *S. fatalis* (Fig. 3A) under laterally directed extrinsic

103   loads (lateral shake) are greater than in any other simulated scenario, and exceed those observed

104   for either *H. serum* or the lion. In both the lion and *H. serum*, the stresses are similar and the

105   laterally directed extrinsic forces largely concentrate von Mises stress around the zygomatics and

106   the rostral region (Fig. 4). However, average values of node displacement under lateral shake

107   loads indicate that *H. serum* experiences considerably lower displacements than the lion or *S.*

108   *fatalis* (Fig. 3B).

109   All the taxa experience lower average von Mises stress values with a jaw-muscle-driven

110   bite (Fig. 3A), but this is particularly true for the skull of *C. crocuta* and *L. pictus* (Fig. 3A).

111   Stresses are lower in this scenario than the others because the primary forces are distributed

112   across the braincase and posterior half of the skull, and the rostrum is relatively unaffected (Fig.

113   4). In contrast, because the extrinsic scenarios have a higher load focus on the anterior half of the

114   skull, the skulls are more prone to bending under the simulated loads, especially in elongated

115   skulls.

116

117   **DISCUSSION**

118   Cortical bone (CB) differs from trabecular bone (TB) in having a higher Young's

119   modulus, and therefore, a high supportable load per unit of surface area. However, it has a lower

120   strain index, which gives it greater stiffness and greater ability to resist torque (16-19).

121   Therefore, the large amount of CB in the rostrum of *S. fatalis* (Fig. 1B; Fig. 2) indicates that,

122   similar to the bone-cracking spotted hyena, it was especially equipped to resist larger and more

123   localized stresses than the rostra of both the living *P. leo* (Fig. 1B; Fig. 2) and the scimitar-

124   toothed *H. serum* (Fig. 1B; Fig. 2). In fact, the three-dimensional simulations of different killing-

125   bite scenarios reveal that the rostrum of *S. fatalis* was better able to withstand loads induced

126   when stabbing prey than that of *H. serum* (Fig. 4). Moreover, within our sample of five large

127   carnivorans, the skull of *S. fatalis* is the only one that exhibits a lesser displacement under a

128   stabbing scenario than under a lateral-shake scenario (Fig. 3B).

129   Contrary to CB, TB has a lower Young's modulus, and the supportable load per unit of

130   surface area is reduced, but TB has a higher strain index that gives it greater flexibility (16-19).

131   Moreover, TB is better than CB in resisting compression and shear (16-19). Accordingly, TB is

132   25% as dense, 10% as stiff, and 500% as ductile as CB (16-19). The small proportion of TB in

133   the skull of *S. fatalis* (Fig. 1B, C; Fig. 2), particularly in the posterior region, suggests that its

134   skull was not optimized for resisting sustained, multidirectional and large loads imposed by

135   struggling prey (Fig. 3; Fig. 4). As demonstrated by previous researchers (e.g., 21), *S. fatalis*

136   probably used its powerfully-built forelimbs (10,22) with hypertrophied dew claws (23,24) to

6

137   bring down and fully immobilize large prey, and then applied one or two quick, strong killing-

138   bites to the throat (e.g., 1,2, 7, 13, 14, 25, 26).

139   In contrast, the large amount of TB in the posterior region of the skull of *P. leo* (Fig.

140   1B,C; Fig. 2) reflects its ability to resist the continuous and repetitive multidirectional loads that

141   might occur during a prolonged 'clamp-and-hold' bite (27,28). Results of the FEA analyses also

142   support the idea that the skulls of lions are better adapted to resist laterally-directed loads than

143   those of the sabertooths. For example, although the skulls of *P. leo* and *H. serum* exhibit a

144   similar level of stress when simulating a lateral-shake scenario (Fig. 3A), the rostrum of *P. leo* is

145   less stressed, above the canines (Fig. 4). Moreover, whereas the skull of *H. serum* experiences

146   slightly lower levels of stress under a stabbing than a lateral-shake scenario (Fig. 3A), the skull

147   of *P. leo* experiences similar levels under both scenarios (Fig. 3A), and the average skull

148   displacement of *P. leo* was much lower under a lateral-shake than a stabbing scenario (Fig. 3B).

149   The rostrum of *H. serum* exhibits an intermediate amount of CB to those of *S. fatalis* and

150   *P. leo* (Fig. 1B,C; Fig. 2), suggesting that the skull of *H. serum* had an intermediate ability to

151   resist high peaks of locally concentrated and unidirectional forces. This is consistent with the

152   results obtained from biomechanical simulations of bilateral canine stabbing, in which *H. serum*

153   experienced levels of stress in between that observed in *S. fatalis* and the three extant taxa (Fig.

154   3B; Fig. 4).

155   On the other hand, as the skull of *H. serum* was also in between both *S. fatalis* and *P. leo*

156   in quantity of TB (Fig. 1B,C), its ability to resist continuous and multidirectional loads also

157   should be intermediate to these two felids. Again, the biomechanical simulations for different

158   prey-killing scenarios support this because the skull of *H. serum* and the lion display similar

7

159   overall levels of stress under a lateral-shake scenario, and considerably less than *S. fatalis* (Fig.

160   3A; Fig. 4).

161   Our results suggest that *H. serum* deployed a predatory behavior among large felids, not

162   previously supported with quantitative data, that was in between the canine-shear-bite of *S.*

163   *fatalis* (or dirktooths in general) and the clamp-and-hold technique of lions (or conical tooths).

164   We argue that, like *S. fatalis*, multiple debilitating slashing bites onto the throat of large prey was

165   the most likely predatory behavior for *H. serum*, and probably for all scimitar-tooths, as

166   originally proposed by previous researchers based on qualitative assessments of morphology

167   (e.g., 7). However, unlike *S. fatalis*, our results suggests that the skull of *H. serum* was less

168   stressed by laterally directed loads, which is consistent with a predatory behavior that regularly

169   subjected the skull to such loads as observed in the lion. In support of this, an analysis of upper

170   canine tooth bending strength in carnivorans found that the canines of *H. serum* were more

171   resistant to bending and presumably fracture under mediolaterally directed loads than were the

172   canines of *S. fatalis* (29).

173   The skull of the scimitar-tooth *H. serum* likely was able to support multidirectional loads

174   incurred by struggling prey more often than was *S. fatalis* because of profound differences in

175   their forelimb morphology. Scimitar-tooths were somewhat cursorial predators in open habitats,

176   whereas dirk-tooths behaved as ambush predators in more closed environments (11).

177   Consequently, the forelimbs of *H. serum* exhibit greater adaptations for speed, while those of *S.*

178   *fatalis* emphasize adaptations for strength. Relative to *S. fatalis*, *H. serum* had less robust humeri

179   (diameter/length), less broad humeral epicondyles, relatively shorter olecranon processes and a

180   longer radius to humerus ratio, all of which are consistent with a reduced mechanical advantage

181   of the forelimb muscles and less muscle mass (30). In addition, although the claws of *H. serum*

182   are compressed and curve-shaped, those of digits II-V are reduced and less retractile than those

183   of *S. fatalis*, indicating an adaptive trade-off in the scimitar tooth between having improved

184   traction for pursuing prey and enhanced grappling ability (31). All of these forelimb

185   characteristics suggest less of a reliance on the forelimbs for immobilization of the prey than was

186   the case for *S. fatalis*, and consequently a need for a craniodental skeleton better equipped to

187   support lateral shaking (12). Therefore, our results suggest a gradient of potential functional

188   adaptations in a group of highly specialized predators from the clamp-and-hold technique of the

189   living lion through *H. serum* to the exceedingly specialized canine-shear-bite of *S. fatalis*.

190   Finally, we note that our analysis of cortical and trabecular bone thickness and

191   distribution in these five carnivorans revealed a previously unrecognized and unique feature of *S.*

192   *fatalis*. Based on the specimen we scanned, *S. fatalis* had an extremely thick skull as evidenced

193   by the coronal sections as well as our quantitative measures (Fig. 1). The combined thickness of

194   CB and TB, as well as CB alone, in the rostrum far exceeds that of any the other four species. At

195   the temporomandibular joint, *S. fatalis, H. serum* and the spotted hyena exhibit greater total bone

196   thickness than the lion, and unlike the lion, much of this thickness is CB rather than TB. Spotted

197   hyenas are capable of cracking large bones with their strong teeth and jaws, and their massive

198   TMJ likely reflects the associated high bite forces (32, 33). Similarly, the extraordinary thickness

199   of the skull of *S. fatalis* in both the rostrum and TMJ suggests an exceptionally large investment

200   in cranial strength in *S. fatalis*, and argues for extremely high bite forces in this cat. Therefore,

201   although both the CB/TB and FE analyses are conducted in a single specimen and might not

202   represent the pattern for the entire species, our results support clear differences in predatory

203   behavior between the scimitar-tooth *H. serum*, and the dirk-tooth *S. fatalis*. In future work, we

204   plan to take advantage of the large sample of *S. fatalis* from the Rancho La Brea tar seeps to

205 explore intraspecific and ontogenetic variability in skull morphology and strength. In addition,

206 given that previous studies have revealed profound interspecific differences among saber-tooth

207 locomotory and predatory strategies among (34), future studies including more species of living

208 felines and other recognized species of *Smilodon* and *Homotherium*, such as their South

209 American vicars, *Smilodon populator* (35) and *Homotherium venezuelensis* (36), could provide

210 additional insights into the diversity of cranial biomechanics in this group of extinct mammalian

211 predators.

212

219

220 **AUTHOR CONTRIBUTIONS:**

221 B.F., B.V.V. designed research; A. P.-R., B.F., S.L., B.V.V. performed research; B.F., B.V.V.,

222 A.P.-R., S.L., wrote the paper.

223 The authors declare no conflict of interest.

224

225 **REFERENCES**

226   1. Bohlin, B. (1940). Food habit of the machaerodonts, with special regard to *S. fatalis*.

227   Bull. Geol. Inst. Upsala 28, 156-174.

228   2. Emerson, S.B., and Radinsky, L. (1980). Functional analysis of sabertooth cranial

229   morphology. Paleobiology 6, 295-312.

230   3. Van Valkenburgh, B. (2007). Deja vu: the evolution of feeding morphologies in the

231   Carnivora. Integr. Comp. Biol. 47, 147-163.

232   4. Andersson, K., Norman, D., and Werdelin, L. (2011). Sabretoothed carnivores and the

233   killing of large prey. PLoS One 6, e24971.

234   5. Palmqvist, P., Martínez-Navarro, B., and Arribas, A. (1996). Prey selection by terrestrial

235   carnivores in a lower Pleistocene paleocommunity. Paleobiology 22, 514-534.

236   6. Kurtén, B. (1968). Pleistocene Mammals of Europe. Weidenfeld and Nicolson,

237   London.

238   7. Martin, L.D. (1980). Functional morphology and the evolution of cats. Transactions of

239   the Nebraska Academy of Sciences 8, 141-154.

240   8. Slater, G.J., and Van Valkenburgh, B. (2008). Long in the tooth: evolution of sabertooth

241   cat cranial shape. Paleobiology 34, 403-419.

242   9. Martin, L.D., Babiarz, J.P., Naples, V.L., and Hearst, J. (2000). Three ways to be a saber-

243   toothed cat. Naturwissenschaften 87, 41-44.

244   10. Meachen-Samuels, J.A., and Van Valkenburgh, B. (2010). Radiographs reveal

245   exceptional forelimb strength in the sabertooth cat, *S. fatalis fatalis*. PLoS one 5, e11412.

246   11. Anyonge, W. (1996). Locomotor behaviour in Plio-Pleistocene sabre-tooth cats: a

247   biomechanical analysis. J. Zool. 238, 395-413.

248   12. Antón, M. (2013). Sabertooth. Indiana University Press.

249   13. Gonyea, W. J. (1976) Behavioral implications of saber-toothed felid morphology.

250   Paleobiology 2, 332-342.

251   14. Akersten, W.A. (1985). Canine function in *S. fatalis* (Mammalia; Felidae;

252   machairodontinae). Natural History Museum of Los Angeles County, Contributions in

253   Science, 356.

254   15. Antón, M., and Galobart, A. (1999). Neck function and predatory behavior in the scimitar

255   toothed cat *H. serum latidens* (Owen). J. Vertebr. Paleontol. 19, 771-784.

256   16. Carter, D.R., and Hayes, W.C. (1977). Compact bone fatigue damage—I. Residual

257   strength and stiffness. J. Biomech. 10: 325-337.

258   17. Guede, D., González, P., and Caeiro, J.R. (2013). Biomecánica y hueso (I): Conceptos

259   básicos y ensayos mecánicos clásicos. Revista de Osteoporosis y Metabolismo Mineral 5,

260   43-50.

261   18. Reddy, S., Dischino, M., and Soslowsky, L.J. (2009). Biomechanics-Part I. Bone

262   Pathology, ed. Khurana J (Humana Press, New York), pp. 61-68.

263   19. Mostakhdemin, M., Amiri, I.S., and Syahrom, A. (2016). Introduction of Bone Study.

264   Multi-axial Fatigue of Trabecular Bone with Respect to Normal Walking, eds.

265   Mostakhdemin M, Amiri IS, Syahrom (Springer Singapore), pp. 1-4.

266   20. Dumont, E. R., Piccirillo, J., & Grosse, I. R. (2005). Finite-element analysis of biting

267   behavior and bone stress in the facial skeletons of bats. *The anatomical record*, *283*(2),

268   319-330.

269   21. McHenry, C.R., Wroe, S., Clausen, P.D., Moreno, K., and Cunningham, E. (2007).

270   Supermodeled sabercat, predatory behavior in *S. fatalis fatalis* revealed by high-

271   resolution 3D computer simulation. P. Natl. Acad. Sci. USA 104, 16010-16015.

272   22. Martín-Serra, A., Figueirido, B., and Palmqvist, P. (2017). Non-decoupled morphological

273   evolution of the fore-and hindlimb of sabretooth predators. J. Anat. 231, 532-542.

274   23. Cox, M., and Jefferson, G.T. (1988). The first individual skeleton of *S. fatalis* from

275   Rancho La Brea. Current Research in the Pleistocene 5, 66-67.

276   24. Bryant, H.N., Russell, A.P., Laroiya, R., and Powell, G.L. (1996). Claw retraction and

277   protraction in the Carnivora: skeletal microvariation in the phalanges of the Felidae. J.

278   Morphol. 229, 289-308.

279   25. Antón, M., Salesa, M.J., Pastor, J.F., Sanchez, I.M., Fraile, S., and Morales, J. (2004).

280   Implications of the mastoid anatomy of larger extant felids for the evolution and

281   predatory behaviour of sabretoothed cats (Mammalia, Carnivora, Felidae). Zool. J. Linn.

282   Soc.-Lond. 140, 207-221.

283   26. Salesa, M.J., Antón, M., Turner, A., and Morales, J. (2005). Aspects of the functional

284   morphology in the cranial and cervical skeleton of the sabre-toothed cat

285   *Paramachairodus ogygia* (Kaup, 1832) (Felidae, Machairodontinae) from the Late

286   Miocene of Spain: implications for the origins of the machairodont killing bite. Zool. J.

287   Linn. Soc.-Lond. 144, 363-377.

288   27. Schaller, G.B. (2009). The Serengeti lion: a study of predator-prey relations. University

289   of Chicago Press.

290   28. Sunquist, M., and Sunquist, F. (2017). Wild cats of the world. University of Chicago

291   Press.

292   29. Valkenburgh, B.V., and Ruff, C.B. (1987). Canine tooth strength and killing behaviour in

293   large carnivores. J. Zool. 212, 379-397.

294   30. Meachen-Samuels, J.A. (2012). Morphological convergence of the prey-killing arsenal of

295   sabertooth predators. Paleobiology 38, 1-14.

296   31. Antón, M., Galobart, A., and Turner, A. (2005). Co-existence of scimitar-toothed cats,

297   lions and hominins in the European Pleistocene. Implications of the post-cranial anatomy

298   of *H. serum latidens* (Owen) for comparative palaeoecology. Quaternary Sci. Rev. 24,

299   1287-1301.

300   32. Kruuk. H. (1972). The Spotted Hyena" a study of predation and social behavior. Chicago;

301   Univ. Of Chicago Press.

302   33. Ravosa, M.J., Kunwar, R., Stock, S.R., and Stack, M.S. (2007). Pushing the limit:

303   masticatory stress and adaptive plasticity in mammalian craniomandibular jonts. J.

304   Experimental Biology 210, 628-641.

305   34. Lewis, M.E., and Lague, MR. (2010). Interpreting sabertooth cat (Carnivora; Felidae;

306   Machairodontinae) postcranial morphology in light of scaling patterns in felids.

307   Carnivoran evolution: new views on phylogeny, form and function. Cambridge

308   University Press, Cambridge, 411.

309   35. Lund, P.W. 1842. Blik paa Brasiliens Dyreverden för sidste Jordomvaeltning. Fjerde

310   Afhandling: Forstsaettelse af Pattedyrene. Danke vidensk. Selsk., 9:137-209.

311   36. Rincón, A. D., Prevosti, F. J., & Parra, G. E. (2011). New saber-toothed cat records

312   (Felidae: Machairodontinae) for the Pleistocene of Venezuela, and the Great American

313   Biotic Interchange. *Journal of Vertebrate Paleontology*, *31*(2), 468-478.

314   37. Marinelli, W. (1938). Der Schlidel von *S. fatalis*, nach der Funktion das Kieferapparates

315   analysiert. Paleobiologica 6, 246-272.

316   38. Rawn-Schatzinger, V. (1992). The scimitar cat, *H. serum serum* cope: osteology,

317   functional morphology, and predatory behavior. Illinois State Museum.

318   39. Marean, C.W., and Ehrhardt, C.L. (1995). Paleoanthropological and paleoecological

319   implications of the taphonomy of a sabertooth's den. J. Hum. Evol 29, 515-547.

320   40. Antón, M., Salesa, M.J., Galobart, A., and Tseng, Z. J. (2014). The Plio-Pleistocene

321   scimitar-toothed felid genus *H. serum* Fabrini, 1890 (Machairodontinae, Homotherini):

322   diversity, palaeogeography and taxonomic implications. Quaternary Sci. Rev. 96: 259-

323   268.

324   41. Schneider, C.A., Rasband, W.S., and Eliceiri, K.W. (2012). NIH Image to ImageJ: 25

325   years of image analysis. Nat. methods 9, 671-675.

326   42. Kikinis, R., Pieper, S.D., and Vosburgh, K.G. (2014). 3D Slicer: a platform for subject-

327   specific image analysis, visualization, and clinical support. Intraoperative imaging and

328   image-guided therapy, ed, Jolesz FA (Springer New York), pp. 277-289.

329   43. Lehmann, L.A., Alvarez, R.E., Macovski, A., Brody, W.R., Pelc, N.J., Riederer, S.J., and

330   Hall, Al. (1981). Generalized image combinations in dual KVP digital radiography. Med.

331   Phys. 8, 659-667.

332   44. Ney, D. R., Fishman, E. K., Magid, D., and Drebin, R.A. (1990). Volumetric rendering of

333   computed tomography data: Principles and techniques. IEEE Computer Graphics and

334   Applications. 10, 24-32.

335   45. Sezgin, M., and Sankur, B. (2004). Survey over image thresholding techniques and

336   quantitative performance evaluation. J. Electron Imaging 13, 146-165.

337   46. Cignoni, P., Callieri, M., Corsini, M., Dellepiane, M., Ganovelli, F., and Ranzuglia, G.

338   (2008). Meshlab: an open-source mesh processing tool. Eurographics Italian Chapter

339   Conference: 129-136.

340   47. Chamoli, U., and Wroe, S. (2011). Allometry in the distribution of material properties

341   and geometry of the felid skull: Why larger species may need to change and how they

342   may achieve it. *Journal of Theoretical Biology*, *283*(1), 217-226.

343   48. Slater, G. J., and Van Valkenburgh, B. (2009). Allometry and performance: the evolution

344   of skull form and function in felids. J. Evolution. Biol. 22, 2278-2287.

345   49. Attard, M.R.G., Chamoli, U., Ferrara, T.L., Rogers, T.L., and Wroe, S. (2011). Skull

346   mechanics and implications for feeding behaviour in a large marsupial carnivore guild:

347   the thylacine, Tasmanian devil and spotted-tailed quoll. J. Zool. 285, 292-300.

348   50. Bourke, J., Wroe, S., Moreno, K., McHenry, C., & Clausen, P. (2008). Effects of gape

349   and tooth position on bite force and skull stress in the dingo (Canis lupus dingo) using a

350   3-dimensional finite element approach. *PLoS One*, *3*(5), e2200.

351   51. Thomason, J.J. (1991). Cranial strength in relation to estimated biting forces in some

352   mammals. Can. J. Zool. 69, 2326-2333.

353   52. Rayfield, E.J. (2007). Finite element analysis and understanding the biomechanics and

354   evolution of living and fossil organisms. Annu. Rev. Earth Planet. Sci. 35, 541-576.

355

356

357

358   **Figure 1**. Amount and distribution of cortical (CB) and trabecular bone (TB). A, *S. fatalis* skull

359   (left); palatal view of thesameskull showing the positions of the ten coronal slices selected for

360   quantifying the area of CB and TB (middle), and representative slice taken at position #8, the

361   temporomandibular joint (right), with CB in yellow and TB in green. B, Bivariate plots of

362   cortical bone area relative to total skull area (RCBT) and trabecular bone area relative to total

363   skull area (RTBT) across the ten coronal slices. C, Bivariate plots of cortical bone area relative to

364   total skull area per slice (RCBS), and trabecular bone area relative to total skull area per slice

365   (RTBS) across the ten coronal slices. The ten slices are: 1, anterior-most point of the canine; 2,

366   posterior-most point of the canine; 3, anterior-most point of the fourth upper premolar; 4,

367   junction between the metacone and paracone of the upper fourth premolar; 5, posterior-most

368   point of the fourth upper premolar; 6, anterior-most point of the squamosal-jugal suture on the

369   zygomatic arch; 7, posterior-most point of the squamosal-jugal suture on the zygomatic arch; 8,

370   temporomandibular joint (TMJ); 9, anterior-most point of the tympanic bulla; 10, anterior-most

371   point of the occipital condyles. The slices defined at interdental gaps are taken at alveolar

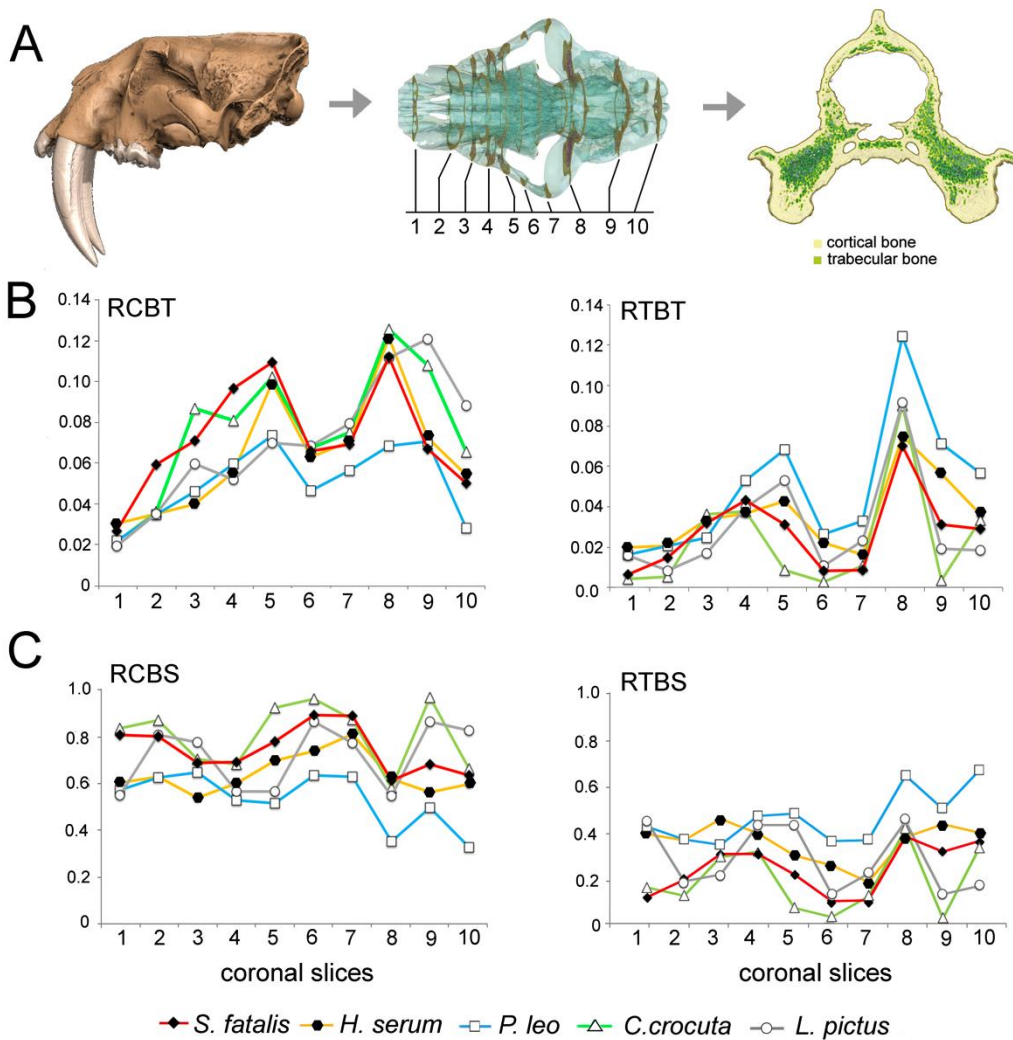372   margins. All the skulls are scaled isometrically to 200 mm from prosthion to inion.

373

374

375

376

377

378

379

380

381

382

383

384

385

386

387

388
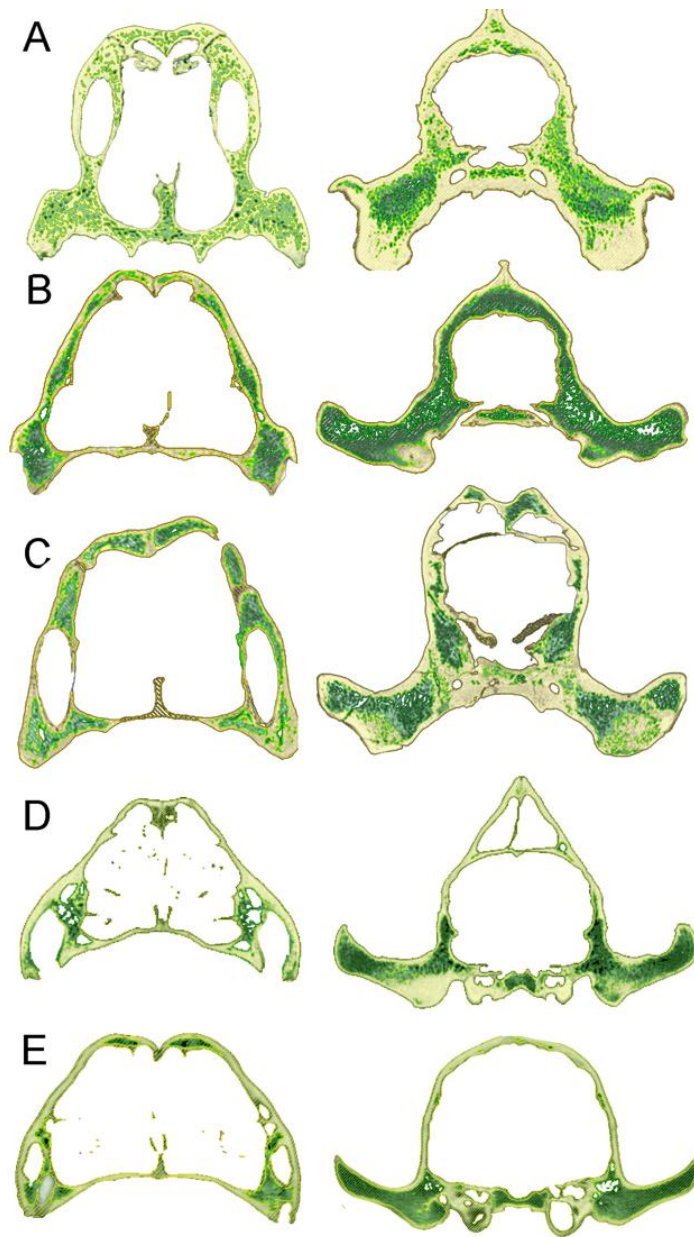
412 **Figure 3**. Finite Element Analysis. A, average (per element) von Mises stress (MPa) for each

413 species in a given loading scenario. B, Average nodal displacement (mm) of the models for each

414 species in a given loading scenario as a proxy for model deformation. Data are for models under

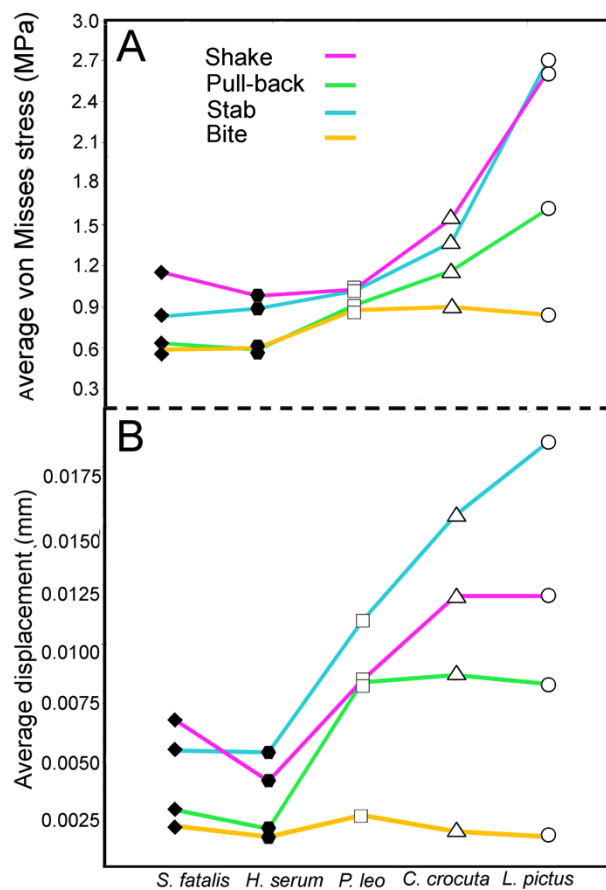415 extrinsic and intrinsic loads during bilateral canine biting.

416

417

418

419

420

421

422

423

424

425

426

427

428

429

430

431

432

433

434

435 **Figure 4**. Von Mises stress contour plots obtained from Finite Element Analysis of the crania of

436 both sabertooths and living carnivores under four loading conditions (stabbing, pull-back, lateral

437 shake, and jaw-powered bite) during bilateral canine biting. See also Figure S2 for the

438 simulations of the extrinsic scenarios including the adductor muscles and a fifth intrinsic

439 scenario considering jaw adductors plus neck muscles. In Figure S3 the results under unilateral

440 canine biting are shown.

441

442
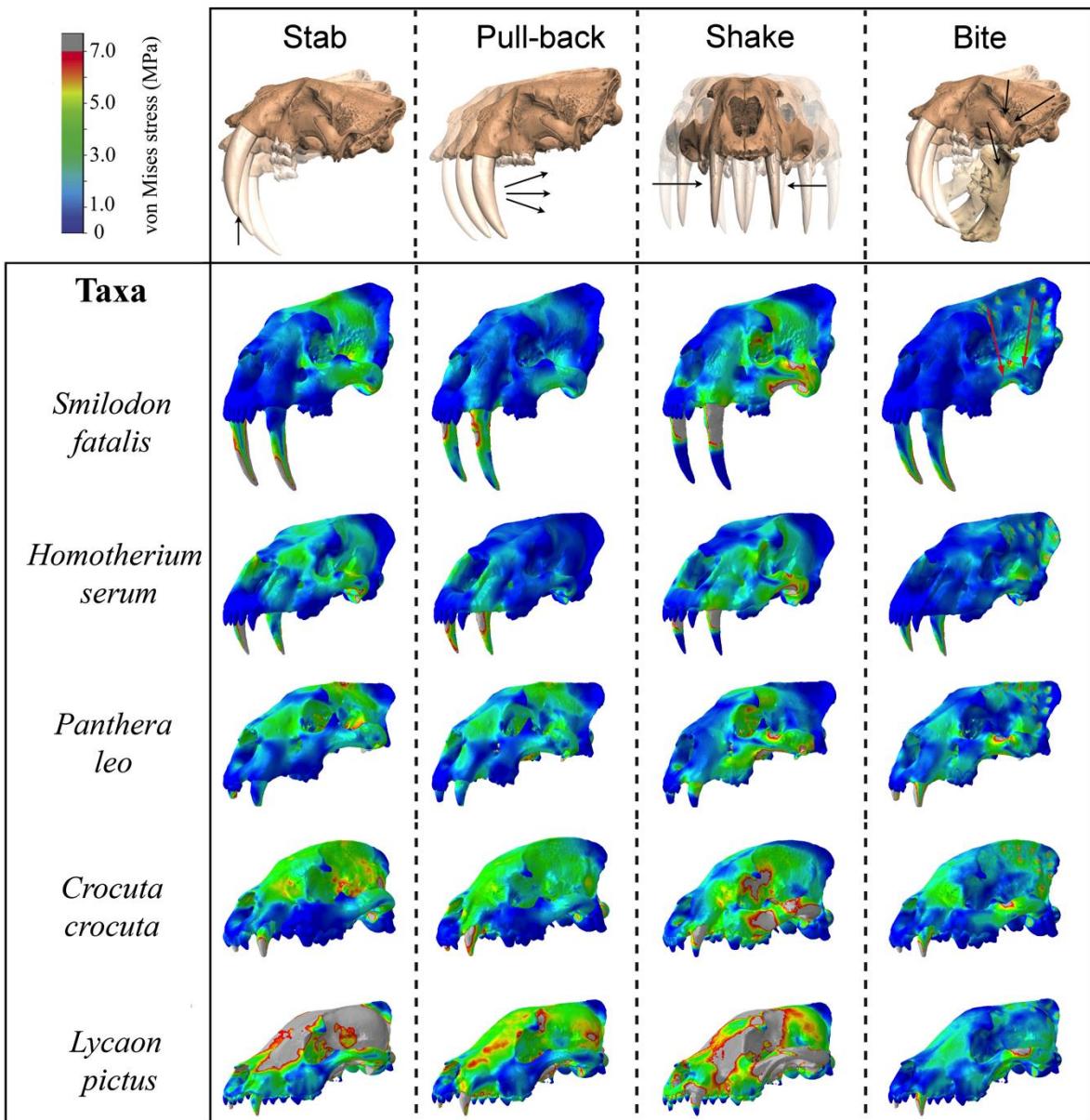
STAR METHODS

Acquisition of CT scans

The crania of the two extinct felids, *H. serum* and *S. fatalis*, as well as three extant carnivorans, African lion (*Panthera leo*), African wild dog (*Lycaon pictus*), and spotted hyena (*Crocuta crocuta*) were CT scanned. All specimens were adults as indicated by fully closed synchondroses and complete tooth eruption. The three extant hypercarnivorous taxa were chosen because researchers have proposed that *H. serum* was more of a carrion-feeder than lion-like active predator (37-39), whereas others have suggested *H. serum* was more similar to pack-hunting canids (12) based on its more gracile limbs and lack of fully retractile claws (31, 40). All specimens were scanned at the University of Texas High-Resolution X-ray Computed Tomography Facility and the scans are available on the UT Digital Morphology website (www. digimorph.org).

Both saber-tooths were scanned at the University of Texas High-Resolution X-ray CT (Facility Archive 1478 for *H. serum* and Facility Archive 0860 for *S. fatalis*). The acquisition properties for *H. serum* were 1024x1024 pixel size for 16-bit TIFF images, 419 kV, 1.8 mA, with voxel size (mm) of 0.1904 (X), 0,1904 (Y), 0.6500(Z) (total slices = 495). The acquisition properties for *S. fatalis* were1024x1024 16-bit TIFF images, 420 kV, 1.8 mA, with voxel size in mm of 0.2143(X), 0.2143 (Y), 0.5000 (Z) (total slices = 629). The specimen of *S. fatalis* (LACMRLP R37376) is from from Rancho La Brea (Los Angeles, California) collected at pit 91, and *H. serum* at (TMM 933-3444) was discovered at Friesenhahn cave (Texas, USA).

We also used extant taxa for comparative purposes, as follows: (i) lion *Panthera leo* (MVZ 117849) of unknown sex as a large pantherine, specimen collected from Skukuza (Kruger

477   Park, Tranvaal, South Africa), and scanned at the University of Texas High-Resolution X-ray CT

478   (Facility Archive 0320), acquisition properties were 512x512 16-bit TIFF images of the whole

479   skull, 420 kV, 1.8 mA, and the voxel size in mm was 0.5273(X), 0.5273 (Y), 1.0000 (Z) (total

480   slices = 406); (ii) spotted hyena, *Crocuta crocuta* (UCMVZ 184551) as a bone-cracker model, a

481   male collected from Masai Mara National Reserve, Kenya, and scanned at the University of

482   Texas High-Resolution X-ray CT (Facility Archives 0277), acquisition properties were 512x512

483   16-bits and converted 8 bits TIFF images, 420 kV, 1.8 mA, with a voxel size in mm of

484   0.3242(X), 0.3242 (Y), 0.5000 (Z) (total slices = 528); (iii) African wild dog, *Lycaon pictus*

485   (USNM 368441), as a pack-hunter hypercarnivore, a male collected in Bechuanaland,

486   Makeleapudi, and scanned at the University of Texas High-Resolution X-ray CT, acquisition

487   properties are 1024x1024 16-bit TIFF images, 419 kV, 1.8 mA, (total slices = 523).

488   Museum abbreviations are as follows: Museum of Vertebrate Zoology at Berkley (MVZ);

489   University of California Museum of Vertebrate Zoology (UCMVZ); United States National

490   Museum of Natural History at Washington DC (USNM); Los Angeles County Museum, Rancho

491   La Brea (LCMRLP); and Texas Memorial Museum (TMM).

492

493   **Quantification and distribution of CB vs TB**

494   The dataset for each of the scanned skulls consisted of a stack of 16-bit TIFF images, all

495   of which were adjusted for brightness and contrast to eliminate background noise using ImageJ

496   (41). All images were normalized at 0.5% and the histogram was adjusted to the range of interest

497   (ROI) using the semiautomatic brightness/contrast tool of ImageJ (41). Subsequently, all images

498   were converted to 8 bits and exported to 3D-slicer (42) to generate the 3D models of each skull.

499   To select the total amount of bone, and to avoid possible overestimations due to Compton and

500 photoelectric effects (43), we used a range of gray values of 70-255 and created a slice with all

501 the bone. Subsequently, we manually added to this layer the relevant low density structures

502 (e.g.,TB) using a range of grey values between 40-70. We decided to use this range of gray

503 values in order to reach a compromise between capturing all the visible and very small

504 trabeculae but avoiding: (i) the oversegmentation of this relevant bony structures; and (ii) the

505 selection of other undesirable artifacts that are a result of Compton and Photoelectric effects; and

506 (iii) the selection of non-relevant small particles. This resulted in a layer with all the information

507 selected between 40-255 but excluding the background noise due to Compton and photoelectric

508 effects (40). Using this layer, we then segmented CB and TB, respectively, as those structures

509 with gray values ranging from approximately 185-255 for CB and 40-185 for TB.

510 For each 3D model of a skull, we selected ten 1-mm thick coronal slices at key points that

511 were homologous in all the species (Fig. 1A). CB and TB were segmented in each of these ten

512 slices excluding petrosal bones and teeth, based on the values of thresholding specified above

513 using 3D-slicer (42). Thus, for each slice, we generated three independent layers, first for all

514 bone, second for the cortical bone (yellow), and third for trabecular bone (green). Each layer was

515 saved as a stack of TIFF images to be imported into imageJ (41). All the CTs were processed

516 using a bicubic interpolation (44) in order to convert anisotropic voxels (in Z direction) to

517 isotropic-sized voxels (the same X,Y,Z values). Afterwards, the stacks for each skull were scaled

518 to a total length of 200 mm from prosthion to inion isometrically and oriented to the same plane

519 in imageJ (41). After converting the stacks into binary, we used the plug-in of ImageJ, 'analysing

520 particles' (45) to obtain the total surface area of CB and TB (including intratrabeuclar spaces),

521 respectively, in each slice.

522   For both fossil specimens, we used semi-automatic thresholding to select the grey values

523   corresponding to the matrix (non-bony) material prior to selecting the ten coronal slices. The

524   values for this thresholding varies across slices and depends upon the nature of matrix infilling.

525   After selecting the slices, we manually segmented them to remove matrix still present inside the

526   trabecular bone of the skull. Damaged trabeculae during the fossilization process in the skulls of

527   both saber-tooths were not observed. Furthermore, the inclusion of the intra-trabecular spaces in

528   the calculation of TB avoids possible (but not visible), very small damaged trabeculae.

529   Therefore, there is not an appreciable potential impact of diagenesis on accuracy of measures of

530   CB and TB in both fossil skulls. Mirroring to compensate for missing structures was done in

531   only a few instances. The exceptions were a few struts of the frontal sinus in *S. fatalis*, and a

532   small portion of the palate of *H. serum*, that were restored by mirroring the preserved

533   counterparts. Restored parts of the skull had a minimum potential impact on the calculation of

534   CB and TB across the skulls.

535   Both three-dimensional surface models were imported into MeshLab (46) in PLY or STL

536   formats (Polygon File Format or the Stanford Triangle Format) for mesh repair, cleaning and

537   simplification.

538   Values of CB and TB were scaled by: i) the sum of CB and TB of the ten slices (i.e., total

539   area of bone quantified across the skulls); and (ii) the total area of CB plus TB of each slice.

540   Both approaches are complementary in the following way: the first approach shows not only the

541   distribution of CB and TB across the skull, but also the heterogeneous distribution of bone across

542   slices; with the second approach the contribution of CB or TB in each slice is shown without

543   regard to the heterogeneous distribution of bone across the skull.

544   The proportion of cortical to trabecular bone tends to decrease with increasing size

545   among felids (47). Therefore, larger species have less cortical bone and more trabecular bone.

546   However, this allometric effect does not affect our results, given that we analyzed the

547   distribution of cortical and trabecular bone across ten functional key points of the skull, rather

548   than just the total amounts of CB and TB. Moreover, both *H. serum* (skull length=326mm) and

549   *S. fatalis* (skull length=322mm) have similar skull sizes to the living lion (skull length=408 mm),

550   and yet they vary greatly in CB/TB across their skulls.

551

552   **Finite Element Analysis**

553   The 3D models of all skulls were imported into Hypermesh 11 (Altair Engineering) for

554   the generation of solid meshes (consisting of approximately 1,000,000 tetrahedral elements per

555   model) and the setting of boundary conditions. All skull models were scaled to the same surface

556   area to allow comparisons of form and function independent of size (48). Material properties for

557   bone and teeth were assigned in Hypermesh based on published values in comparable studies on

558   mammalian carnivores (bone: E = 13.7 (cortical) & 9.29 (trabecular) GPa, $v = 0.30$, teeth: E =

559   38.6.0 GPa, $v = 0.4$) (46-48). All materials were treated as isotropic and homogenous.

560   Five different functional scenarios were tested. Three extrinsic scenarios: (i) stabbing

561   prey using both canine teeth with a dorsally directed extrinsic force of 500 N applied to the tips

562   of both canines (stab in Figure 4); (ii) pulling the head posteriorly with both canine teeth

563   embedded in the prey and an extrinsic force of 500 N distributed over the posterior edge of the

564   canines (pull-back in Figure 4); and (iii) shaking the head laterally while holding prey with both

565   canine teeth and an extrinsic force of 500 N applied to the left side of both canines (shake in Fig.

566   4). The extrinsic force (total of 1000 N for each scenario) was selected based on reported

567   magnitudes for neck-muscle-driven bite force (21). For the extrinsic feeding scenarios,

568   constraints were placed on the articular surface of the squamosal (five nodes on each side), as

569   well as the occipital condyle (ten nodes) to restrain the model from movement in x-, y- and z-

570   directions to simulate the fixed contact of the skull with other skeletal elements (i.e. mandible

571   and vertebral column).

572   A further intrinsic scenario (iv) was analyzed that simulated a jaw adductor muscle-

573   driven biting assuming a gape angle of 25 degrees following (50). For this purpose, jaw adductor

574   muscle forces were estimated using the attachment area of each muscle (Fig. S1), as a proxy for

575   physiological cross-section area and multiplying it by an isometric muscle stress value of 0.3 N/

576   mm2 (51). This approach likely underestimates the total muscle force and resulting bite forces

577   due to simplifying a three-dimensional muscle volume to a two-dimensional surface area.

578   However, given the lack of accurate data on muscle volume and architecture for fossil

579   carnivorans, this approach provides a repeatable method for estimating muscle force across taxa

580   and permits functional comparisons. Models in this scenario were constrained at the tip of the

581   canine tooth (one node on each side) to restrain the model from movement in x- and y- direction

582   (i.e. medial/lateral and anterior/posterior), but not in z-direction to simulate some penetration of

583   the canines into the prey during biting.

584   In addition, a combined functional scenario (v) was tested simulating the simultaneous

585   action of the jaw closing muscles and the neck musculature. For this, an extrinsic force of 500 N

586   on each side was added to the aforementioned intrinsic scenario and distributed over the back of

587   the skull and the mastoid region. The magnitude of the load was selected to be the same as with

588   the extrinsic scenarios, based on reported magnitudes for neck-muscle-driven bite force (21). The

589   directions of the muscle forces were determined by creating vectors between the muscle origin

590   and insertion sites, using corresponding mandibular models or simplified templates, where this

591   was not possible (i.e. postcranial muscles).

592   Further to these scenarios and to simulate the combined action of the jaw adductor

593   muscles and external forces (i.e., stab, pull-back, lateral shake) experienced during movement of

594   the prey and/or the head, all extrinsic scenarios were further analyzed with adductor loads active.

595   Cranial (adductor) and postcranial muscles were considered separately in the functional analyses

596   to evaluate their contribution to the stress behavior. However, combined loads of the cranial and

597   postcranial musculature were tested as well (see supplementary Figure S2). Results show that the

598   combined muscle forces have very little effect on the stress distribution. The simulations were

599   performed during bilateral (Figs. 3,4) and unilateral (Fig. S3) canine biting. All models were

600   subsequently imported into Abaqus 6.141 (Simulia) for analysis and post-processing.

601   Biomechanical performance for the FE models was assessed via contour plots of Von Mises

602   stress distribution, reaction forces, and average Von Mises stress and displacement values per

603   element with the top 1% of values removed to avoid the influence of individual stress

604   singularities at constrained or loaded nodes. The jaw-joint reaction forces quantify the internal

605   force generated at node constraints (TMJ), the Von Mises (VM) stress distributions represent a

606   function that measures how stress distorts a material, and the displacement values per element

607   measure how the elements of the mesh are displaced when a given force is applied (52).